Analysis, Design, and Control of an Omnidirectional Mobile Robot in Rough Terrain

Martin Udengaard
e-mail: mru@alum.mit.edu

Karl Iagnemma
e-mail: kdi@mit.edu

Department of Mechanical Engineering,
Massachusetts Institute of Technology,
77 Massachusetts Avenue,
Cambridge, MA 02139

An omnidirectional mobile robot is able, kinematically, to move in any direction regardless of current pose. To date, nearly all designs and analyses of omnidirectional mobile robots have considered the case of motion on flat, smooth terrain. In this paper, an investigation of the design and control of an omnidirectional mobile robot for use in rough terrain is presented. Kinematic and geometric properties of the active split offset caster drive mechanism are investigated along with system and subsystem design guidelines. An optimization method is implemented to explore the design space. The use of this method results in a robot that has higher mobility than a robot designed using engineering judgment. A simple kinematic controller that considers the effects of terrain unevenness via an estimate of the wheel-terrain contact angles is also presented. It is shown in simulation that under the proposed control method, near-omnidirectional tracking performance is possible even in rough, uneven terrain. [DOI: 10.1115/1.4000214]

1 Introduction

Mobile robots are finding increasing use in military [1], disaster recovery [2], and exploration applications [3]. These applications frequently require operation in rough, unstructured terrain. Currently, most mobile robots designed for these applications are tracked or Ackermann-steered wheeled vehicles. Methods for controlling these types of robots in both smooth and rough terrain were well studied [4–6]. While these robots can perform well in many scenarios, navigation in cluttered, rocky, or obstacle-dense urban environments can be difficult or impossible. This is partly due to the fact that traditional tracked and wheeled robots must reorient to perform some maneuvers such as lateral displacement. Omnidirectional mobile robots could potentially navigate faster and more robustly through cluttered urban environments and over rough terrain, due to their ability to track nonsmooth motion profiles.

An omnidirectional mobile robot is able, kinematically, to move in any direction regardless of current pose. Previous researchers proposed and developed omnidirectional mobile robots employing a wide variety of wheel types including roller [7,8], Mecanum [9,10], and spherical wheels [11,12]. Other researchers studied the kinematics of these types of robots [13–15].

Roller wheel designs, as shown in Fig. 1, employ small rollers along the outer edge of a "primary" wheel to allow traction in the wheel's longitudinal direction, and free rolling in the lateral direction. Omnidirectional motion is obtained by orienting several of these wheels in different directions. These wheels are inexpensive, easy to control, and operate well in flat, indoor environments.

Mecanum wheels are similar to roller wheels in that they employ rollers along the outer edge of a wheel; however, the rollers are aligned at an angle to produce angular contact forces with the ground. Robots equipped with four Mecanum wheels, as shown in Fig. 2, can produce omnidirectional motion (see Fig. 3). Again, these wheel types have proved to be simple to control, and effective on flat, indoor terrain.

Roller and Mecanum wheels are unsuitable for outdoor environments, where debris can clog the rollers and alter the friction characteristics of the wheels [16]. Also, the (relatively) small rollers on the edge of each primary wheel can be subjected to significant loads, which can lead to high ground pressure and large sinkage in deformable outdoor terrain.

Spherical wheel designs, as shown in Fig. 4, employ frictional drive rollers to allow rolling in any direction. Since the drive rollers rely on friction to transmit energy to the wheel, debris could potentially foul the transmission mechanism in rough, outdoor environments. Due to the two-dimensional curvature of the sphere, the contact patch is smaller than that of a traditional wheel, leading to increased ground pressure, given the same ground reaction force.

Near-omnidirectional motion was achieved using steerable wheels [17]. As shown in Fig. 5, these designs have a wheel mounted to an orthogonal steering actuator. The steering actuator can rotate the wheel to orient it in any planar direction. These wheels can employ standard tires, and have proven effective in outdoor environments. However, they are not truly omnidirectional (i.e., the resulting vehicle kinematics are subject to nonholonomic constraints) since they must undergo wheel slip and/or scrubbing to change direction. This can result in deteriorated path tracking and substantial energy loss. Note that similar designs based on offset caster wheels do allow omnidirectional motion with standard tires [18]. Analysis of this design has been studied extensively for operation on flat ground.

An omnidirectional mobile robot driven by active split offset casters (ASOCs) was initially proposed in Ref. [19] for use in structured, indoor environments. ASOC drives employ conventional wheel designs that do not rely on frictional contact, and are thus potentially suitable for use in dirty, outdoor environments. They also can be designed with little constraint on wheel diameter and width, and thus, can potentially tolerate large loads with low ground pressure. Finally, ASOC modules can be integrated with suspension systems that allow for traversal of uneven terrain [20]. Therefore, ASOC-driven omnidirectional mobile robots hold promise for use in rough, unstructured environments.

In this paper, an investigation of the design and control of an ASOC-driven omnidirectional mobile robot for use in rough terrain is presented. This paper is organized as follows: In Sec. 2, kinematic and geometric properties of the drive mechanism are analyzed, in Sec. 3, guidelines for robot design are presented, and an optimization method is implemented to explore the design space, and in Sec. 4, a simple kinematic controller that considers the effects of terrain unevenness via an estimate of the wheel-terrain contact angles is presented. These analyses can be used as

Contributed by the Mechanisms and Robotics Committee of ASME for publication in the JOURNAL OF MECHANICAL DESIGN. Manuscript received November 23, 2008; final manuscript received August 24, 2009; published online November 3, 2009. Assoc. Editor: Panos Y. Papalambros.

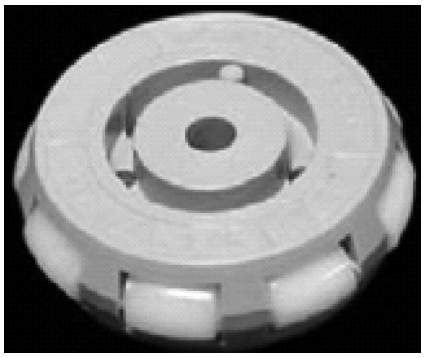

Fig. 1 An example of a sliding wheel(from Ref. [8])

design guidelines for the development of an omnidirectional mobile robot that can operate in unstructured environments. The optimization method is shown to generate design parameters for a robot that has higher mobility than a robot designed using engineering judgment. It is shown in simulation that under the proposed control method, near-omnidirectional tracking performance is possible even in rough, uneven terrain.

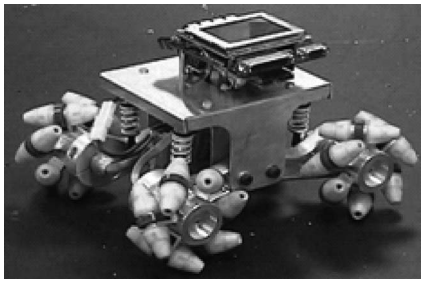

Fig. 2 An example of a robot using four Mecanum wheels (from Ref. [9])

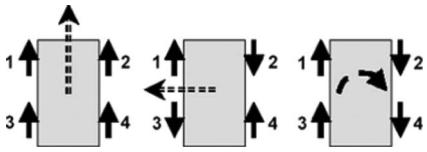

Fig. 3 A schematic showing the omnidirectional capabilities of a Mecanum wheel driven omnidirectional robot (from Ref. [9]). The solid arrows indicate the driven direction of each wheel, and the dashed arrows indicate translation and rotation of the robot.

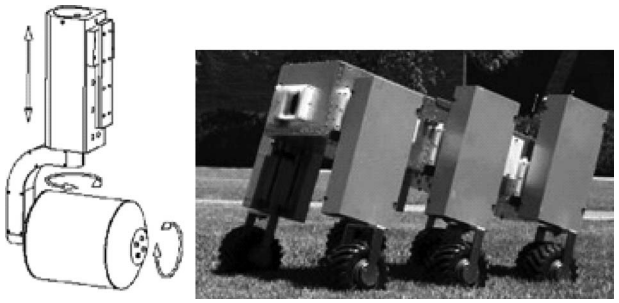

Fig. 5 A schematic showing a steerable wheel (left), and its use on an outdoor mobile robot (right) (from Ref. [17])

2 The ASOC

ASOC drive modules possess the ability to achieve omnidirectional motion via a driven wheel pair. Figure 6 shows the ASOC module considered in this study. The assembly consists of a split wheel pair, a connecting axle, and an offset link connecting the wheel pair to the mobile robot body. Each wheel is independently driven about the axis θ. The axle connecting the wheel pair can pivot about the axis β. The axle pivot can be passive or active, and allows the wheel pair to adapt to terrain unevenness, therefore increasing the likelihood of continuous terrain contact for each wheel, even during travel on rough terrain. The wheel pair/axle assembly rotates about axis α. As with the axle pivot, the assembly rotation axis can also be active or passive. This axis connects the ASOC module to a robot body or a passive or active suspension element. L_{offset} is the distance between the axis α and the axis θ. L_{split} is the distance between the wheels.

By independently controlling each wheel's velocity, an ASOC module can produce arbitrary (planar) translational velocities at a point along its α axis [19]. While this design allows wheel motion with a much lower level of scrubbing than previous designs, some scrubbing will still occur as the wheels have finite width. Two or more ASOCs attached to a rigid robot body can thus produce arbitrary translational and rotational robot velocities. Therefore, an ASOC-driven omnidirectional robot must minimally employ two ASOC modules, and can employ more to meet other design requirements related to thrust, ground pressure, tip-over stability, etc. Note that passive or active casters can also be used to augment ASOC modules to meet these requirements.

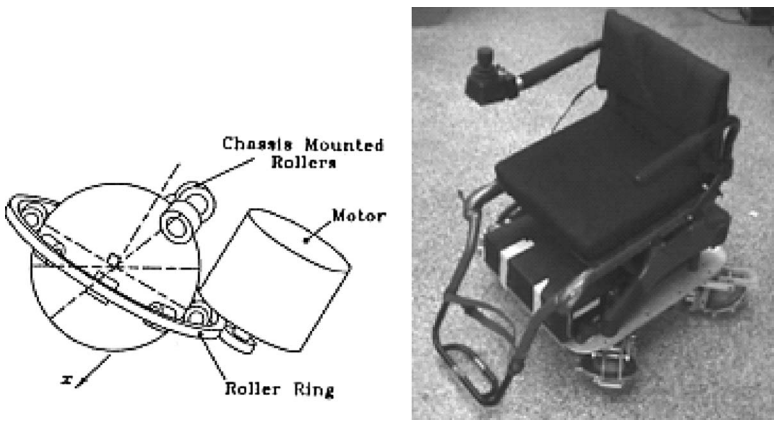

Fig. 4 A schematic showing a spherical wheel (left), and its use on an omnidirectional wheelchair (right) (from Ref. [12])

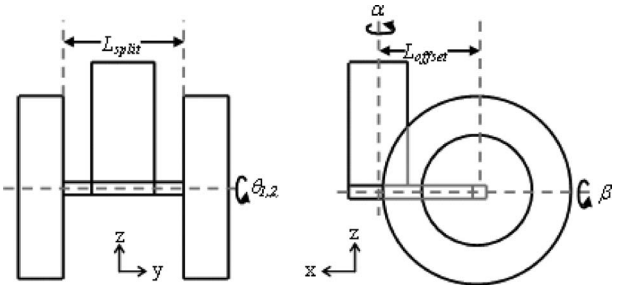

Fig. 6 Active split offset caster wheel assembly front view (left) and side view (right)

2.1 Isotropy Analysis. Path following in rough terrain may require a robot to quickly change its direction of travel. All holonomic omnidirectional mobile robots are kinematically able to instantaneously move in any planar direction. However, while some omnidirectional mobile robots exhibit preferred directions of travel, others exhibit equal mobility characteristics in all directions. Such robots are said to exhibit "isotropic mobility." Hence, isotropy is used to quantify the system's omnidirectional mobility.

Kinematic isotropy is defined as the condition in which a robot possesses a constant input velocity/output velocity ratio for all possible output velocity directions [18]. An isotropy metric is a measure of how near a robot is to the isotropy condition, and increases from 0.0 for a singular configuration (i.e., purely anisotropic, or nonomnidirectional) to 1.0 for kinematic isotropy. Previous studies showed the isotropy calculations for Mecanum [21] and caster wheels [22]. Ideally, an omnidirectional mobile robot should possess a metric value of 1.0 for all joint space configurations, and thus, not exhibit a preferred direction of travel. This simplifies path planning and navigation by eliminating the effect of robot orientation on movement capability. The output directions considered in this study are two planar translations in the robot body frame, and rotation about the robot body frame z-axis. The isotropy metric for a given robot configuration can be computed as the inverse of the condition number of the Jacobian matrix relating the driving module velocities to the robot body velocities [18]. The isotropy metric can be averaged over the entire configuration space (in this case, the rotation angles between each ASOC and the body α) to yield an average measure of performance that could be used to compare candidate omnidirectional mobile robot designs.

2.2 Effect of ASOC Geometric Parameters on Isotropy. To analyze the effects of ASOC module kinematic parameters on isotropy, variations in the wheel radius L_{offset}, and L_{split} were analyzed over a range of values that represent a practical omnidirectional robot design space. The Jacobian from wheel rotational velocities to α axis translational velocities in the ASOC frame is

$$\begin{bmatrix} v_{\text{long}} \\ v_{\text{lat}} \end{bmatrix} = \begin{bmatrix} \frac{R_{\text{wheel}}}{2} & \frac{R_{\text{wheel}}}{2} \\ \frac{R_{\text{wheel}} \cdot L_{\text{offset}}}{L_{\text{split}}} & -\frac{R_{\text{wheel}} \cdot L_{\text{offset}}}{L_{\text{split}}} \end{bmatrix} \begin{bmatrix} \dot{\theta}_1 \\ \dot{\theta}_2 \end{bmatrix} \quad (1)$$

where v_{long} and v_{lat} are the longitudinal (x) and lateral (y) ASOC axis translational velocities, respectively (see Fig. 6). The wheel radius appears in each term exactly once, and cancels out when the ratios of the eigenvalues are computed, thus, the module isotropy is independent of the wheel radius.

In Fig. 7, a plot of isotropy is shown as a function of L_{offset} and L_{split}. An isoheight exists at an isotropy value of 1.0. This isoheight occurs at $L_{\text{split}}/L_{\text{offset}}=2.0$. The sensitivity of isotropy to perturbations in L_{split} and L_{offset} is relatively high; a 10% change in L_{split} or L_{offset} decreases the isotropy metric value by up to 45% for small ASOC module sizes.

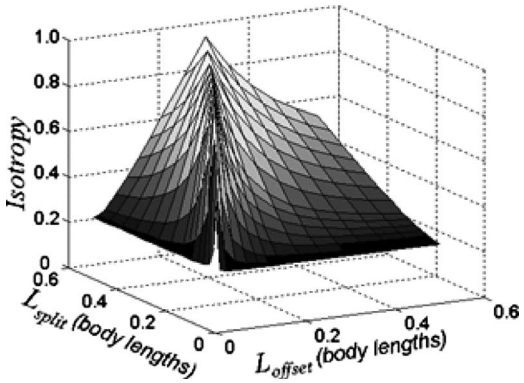

Fig. 7 Mean isotropy for a four ASOC omnidirectional robot

In Fig. 8, a plot of isotropy values over a range of $L_{\text{split}}/L_{\text{offset}}$ ratios can be seen. There exists a single isotropy value for each $L_{\text{split}}/L_{\text{offset}}$ ratio, indicating that isotropy is not an independent function of both L_{split} and L_{offset}. This is a useful insight for omnidirectional robot design. This also explains the sensitivity of isotropy to changes in L_{split} and L_{offset} for small ASOC modules sizes, since a unit change in L_{split} or L_{offset} results in a relatively large change in $L_{\text{split}}/L_{\text{offset}}$ for small parameter values. As shown in Eq. (1), L_{split} and L_{offset} only appear as a ratio, and the Jacobian becomes isotropic (i.e., all eigenvalues are equal) when the ratio of L_{split} to L_{offset} is equal to 2.0.

2.3 Effect of ASOC Module Location on Isotropy. The relative location of ASOC modules with respect to one another also affects isotropy. A vehicle with three modules, shown in Fig. 9, was chosen for analysis. A plot of isotropy as a function of

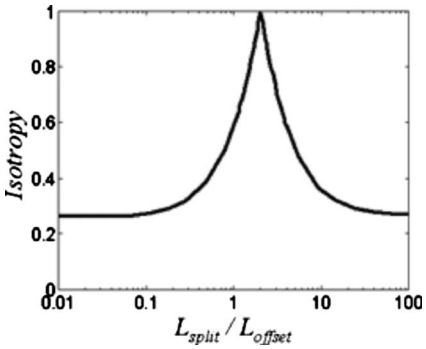

Fig. 8 Average isotropy for an omnidirectional mobile robot driven by three ASOC modules as a function of $L_{\text{split}}/L_{\text{offset}}$

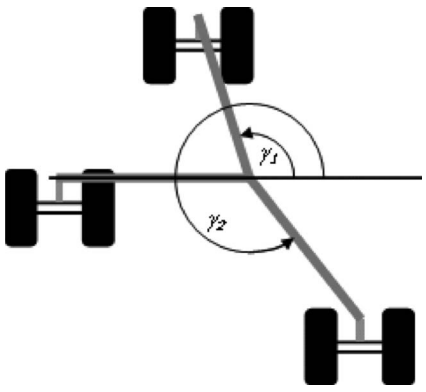

Fig. 9 Top view of representative vehicle for ASOC location analysis

relative ASOC angular location is presented in Fig. 10. Each ASOC had an L_{split}/L_{offset} ratio of 2.0. ASOC physical interference was neglected.

The Jacobian of a three ASOC omnidirectional mobile robot is shown in Eq. (2). Analysis shows that maximum isotropy values (1.0) are obtained when the ASOC modules are evenly spaced, and $L_{split}/L_{offset}=2.0$. The value drops to 0 for the degenerate case where all ASOC modules coincide. A similar phenomenon is observed for robots with any number of ASOC modules. Thus, to maximize isotropy, ASOC modules should be equally spaced

$$J' = \frac{1}{3}\begin{bmatrix} \frac{\cos(\alpha_1)}{2} - \frac{L_{offset}\sin(\alpha_1)}{L_{split}} & \frac{\sin(\alpha_1)}{2} + \frac{L_{offset}\cos(\alpha_1)}{L_{split}} \\ \frac{\cos(\alpha_1)}{2} + \frac{L_{offset}\sin(\alpha_1)}{L_{split}} & \frac{\sin(\alpha_1)}{2} - \frac{L_{offset}\cos(\alpha_1)}{L_{split}} \\ \frac{\cos(\alpha_2)}{2} - \frac{L_{offset}\sin(\alpha_2)}{L_{split}} & \frac{\sin(\alpha_2)}{2} + \frac{L_{offset}\cos(\alpha_2)}{L_{split}} \\ \frac{\cos(\alpha_2)}{2} + \frac{L_{offset}\sin(\alpha_2)}{L_{split}} & \frac{\sin(\alpha_2)}{2} - \frac{L_{offset}\cos(\alpha_2)}{L_{split}} \\ \frac{\cos(\alpha_3)}{2} - \frac{L_{offset}\sin(\alpha_3)}{L_{split}} & \frac{\sin(\alpha_3)}{2} + \frac{L_{offset}\cos(\alpha_3)}{L_{split}} \\ \frac{\cos(\alpha_3)}{2} + \frac{L_{offset}\sin(\alpha_3)}{L_{split}} & \frac{\sin(\alpha_3)}{2} - \frac{L_{offset}\cos(\alpha_3)}{L_{split}} \end{bmatrix} \cdots$$

$$\begin{bmatrix} \frac{\sin(\alpha_1)}{2} + \frac{L_{offset}\cos(\alpha_1)}{L_{split}} \\ \frac{\sin(\alpha_1)}{2} - \frac{L_{offset}\cos(\alpha_1)}{L_{split}} \end{bmatrix}$$

$$\begin{bmatrix} \cos(\gamma_1)\left(\frac{\sin(\alpha_2)}{2} + \frac{L_{offset}\cos(\alpha_2)}{L_{split}}\right) - \sin(\gamma_1)\left(\frac{\cos(\alpha_2)}{2} - \frac{L_{offset}\sin(\alpha_2)}{L_{split}}\right) \\ \cos(\gamma_1)\left(\frac{\sin(\alpha_2)}{2} - \frac{L_{offset}\cos(\alpha_2)}{L_{split}}\right) - \sin(\gamma_1)\left(\frac{\cos(\alpha_2)}{2} + \frac{L_{offset}\sin(\alpha_2)}{L_{split}}\right) \\ \cos(\gamma_2)\left(\frac{\sin(\alpha_3)}{2} + \frac{L_{offset}\cos(\alpha_3)}{L_{split}}\right) - \sin(\gamma_2)\left(\frac{\cos(\alpha_3)}{2} - \frac{L_{offset}\sin(\alpha_3)}{L_{split}}\right) \\ \cos(\gamma_2)\left(\frac{\sin(\alpha_3)}{2} - \frac{L_{offset}\cos(\alpha_3)}{L_{split}}\right) - \sin(\gamma_2)\left(\frac{\cos(\alpha_3)}{2} + \frac{L_{offset}\sin(\alpha_3)}{L_{split}}\right) \end{bmatrix} \quad (2)$$

2.4 Effect of Loss of Wheel Contact on Isotropy. When traversing rough terrain, loss of contact may occur between the wheels and the ground. In this case, system mobility will be decreased. An analysis of the isotropy of robots without full ground contact is presented in Table 1. For comparison, robots with two, three, and four ASOC modules are examined. Each ASOC is allowed to possess full, partial (i.e., one wheel on the ground), or no ground contact. It is assumed that the ASOC modules are equally spaced and have $L_{split}/L_{offset}=2.0$.

As expected, loss of wheel contact causes reduced isotropy due to a loss of full controllability of the ASOC modules. It can be observed that a four ASOC robot with one module that has completely lost terrain contact does not perform as well as a three

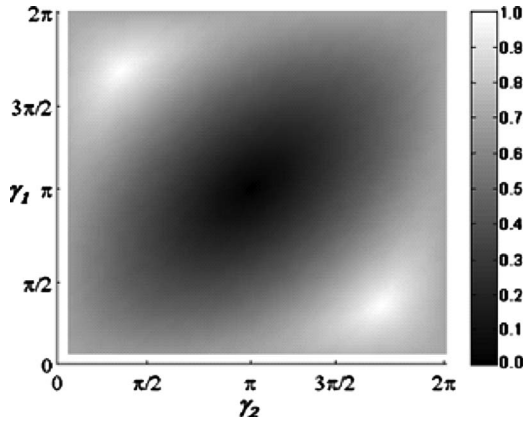

Fig. 10 Isotropy as a function of ASOC module relative location

Table 1 Effect of loss of wheel contact on isotropy

Total No. of ASOCs	No. of no contact ASOCs	No. of partial contact ASOCs				
		0	1	2	3	4
2	0	1.000	0.464	0.000	N/A	N/A
3	0	1.000	0.706	0.504	0.270	N/A
	1	0.577	0.367	0.000	N/A	N/A
4	0	1.000	0.791	0.656	0.544	0.399
	1	0.707	0.574	0.482	0.259	N/A
	2	0.414	0.265	0.000	N/A	N/A

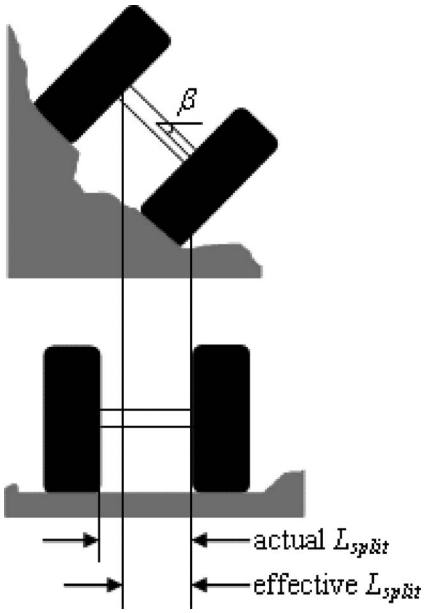

Fig. 11 ASOC module on flat and rough terrain. Rough terrain can cause the module to pivot about the β axis, decreasing the effective L_{split}.

ASOC vehicle in full contact. This is due to the fact that the three ASOC robot has equally spaced ASOC modules. Also, given an identical number of wheels without terrain contact (e.g., 0 no contact and 2 partial contact versus 1 no contact and 0 partial contact), a robot generally has higher isotropy when terrain contact is lost on the same ASOC, since more modules remain fully engaged with the ground. It should be noted that a module with only one wheel contacting the ground cannot produce an arbitrary planar velocity vector at a point along its α axis. In some scenarios this makes omnidirectional motion impossible to achieve. Generally, when a wheel loses contact with the ground, free rotation of the ASOC module about the α axis will tend to orient the wheel in the direction of robot travel. This rotation produces some scrubbing and is not directly controllable. The isotropy loss from partial contact ASOC modules reinforces the importance of the β axis axle pivot (see Fig. 6).

Finally, a vehicle with a greater number of ASOCs will have a relatively smaller decrease in isotropy for each lost wheel contact, but may have increased difficulty keeping all wheels in contact with the ground due to increased suspension complexity. Introduction of additional modules may also increase mass while decreasing the allowable wheel size and available battery mass, given a fixed overall system mass.

2.5 Effect of Terrain Roughness on Isotropy. Isotropy of an omnidirectional robot can also be affected by terrain roughness. Variation in terrain inclination among ASOC modules, or among ASOC module wheel pairs, causes a change in the effective value of L_{split} with respect to the body frame, which yields a change in L_{split}/L_{offset}, and thus, a change in isotropy (see Fig. 11). Axis β allows ASOC wheels to maintain contact during travel on uneven terrain. It should be noted that for very large changes in terrain height between modules, a suspension mechanism with higher displacement capability (such as an independent wheel suspension) would be necessary to ensure that each module can maintain ground contact.

In theory, L_{split} could be modified as a function of terrain inclination via an active, extensible axle to cause the effective L_{split}/L_{offset} ratio to always remain near 2.0, thus, yielding good isotropy characteristics on rough terrain. In practice, however, such a design would be cumbersome and impractical. Thus, it is useful to examine the effects of terrain inclination on robot isotropy.

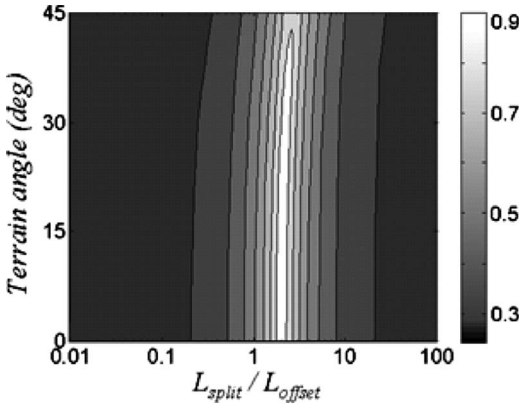

Fig. 12 Mean isotropy as a function of L_{split}/L_{offset} and terrain angle

In Fig. 12, a contour plot is presented of the average isotropy over a range of static robot configurations and terrain angles. The vehicle in this analysis had equally spaced ASOCs. The results are independent of the number of ASOC modules. The terrain angle was varied for each ASOC independently in a full factorial analysis over each terrain angle range. It can be seen that the L_{split}/L_{offset} ratio with the largest isotropy value increases with the maximum terrain angle. Larger angles decrease the effective ratio, and thus, the "true" ratio must increase. Maximum average isotropy also decreases slightly with increasing terrain angle. Table 2 summarizes these findings.

3 Design of an Omnidirectional Mobile Robot for Rough Terrain

The class of robots analyzed in this paper is man-portable, battery powered mobile robots with a maximum enclosed envelope of 1 m^3, and maximum mass of 65 kg. The primary design objective is to maximize traversable distance over a range of outdoor terrain types while maintaining a high level of mobility. Here, mobility is quantified by the system kinematic isotropy, the ability of an ASOC module to maintain ground contact, and the maximum traversable obstacle height. The robot must operate under its own power, and therefore, should maximize mass efficiency to increase its battery payload. It should also minimize power loss from motion resistance in deformable terrain. Factors influencing the design space include wheel width, wheel radius, ASOC split and offset lengths, and the number and relative location of ASOC modules. Geometric constraints that bound the allowable design space must also be considered.

Figure 13 shows an illustration of an omnidirectional mobile robot, driven by four ASOC modules. This is a representative configuration that will be considered in this work; however, the following analysis is general, and applies to robots with N ASOC modules.

Table 2 Effect of terrain on isotropy

Terrain angle range (deg)	Max isotropy	Optimum L_{split}/L_{offset} ratio
0 (flat)	1.000	2.00
0–15	0.987	2.05
0–30	0.950	2.27
0–45	0.895	2.70

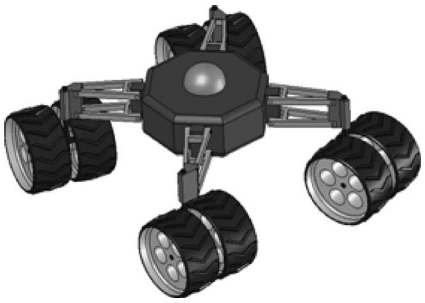

Fig. 13 Illustration of an ASOC-driven omnidirectional mobile robot. This robot has four ASOC modules spaced at 90 deg intervals.

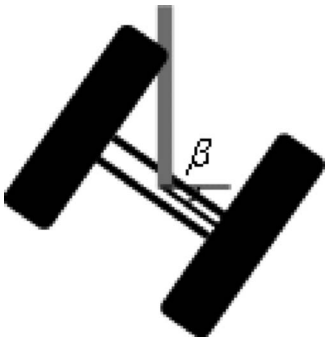

Fig. 15 Rear view of ASOC with wheel-shaft interference

3.1 Geometric Constraints. The unique geometry of the ASOC and the large range of motion of each module constrain the size of some mechanical components. Potentially, a control algorithm could utilize the robot's redundancy to relax these constraints (by ensuring that wheel pairs are never directly oriented toward each other, for example). However, such an algorithm would likely reduce overall system mobility. Therefore, a geometric analysis of the ASOC module workspace is presented here.

3.1.1 ASOC Workspace Analysis. The maximum allowable wheel size that does not risk inter-ASOC interference can be calculated by simple geometric analysis of the module workspace. As seen in Fig. 14, the minimum distance between adjacent ASOC axes d_a must be at least twice the maximum radius of the ASOC module workspace $r_{\text{workspace}}$. This radius is the distance from the vertical axis to the most distal point on the wheel

$$r_{\text{wheelenvelope}} = \sqrt{(L_{\text{offset}} + r_{\text{wheel}})^2 + (0.5L_{\text{split}} + t_{\text{wheel}})^2} \tag{3}$$

where L_{offset} and L_{split} are the ASOC split and offset lengths, respectively, and r_{wheel} and t_{wheel} are the wheel radius and width, respectively.

3.1.2 Maximum Pivot Angle Analysis. In rough terrain, the passive pivot axis (see Fig. 6) allows the ASOC wheels to conform to terrain unevenness. A potential limiting factor of the pivot axis travel is the wheel-shaft interference (see Fig. 15).

The maximum allowable rotation angle of β can be calculated as the angle at which the inner rim of the wheel intersects the vertical shaft that connects the module to the robot body. This occurs when

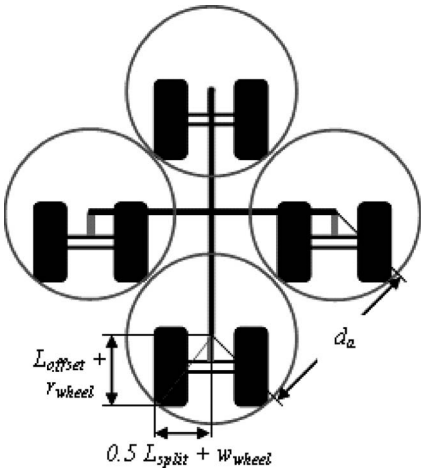

Fig. 14 The circles represent the boundaries of the ASOC module workspace. To avoid ASOC interference, they should not intersect.

$$0.5L_{\text{split}} \cos \beta = r_{\text{wheeleffective}} \sin \beta \tag{4}$$

where β is the angle of the pivot rotation, and $r_{\text{wheeleffective}}$ is the vertical distance from the center of the wheel to the section of the rim that intersects the shaft, as shown in Fig. 16.

The value is calculated as

$$r_{\text{wheeleffective}} = \sqrt{r_{\text{wheel}}^2 - L_{\text{offset}}^2} \tag{5}$$

Note that when $L_{\text{offset}} > r_{\text{wheel}}$, the shaft and wheel cannot interfere. However, such configuration could allow obstacles to collide with the ASOC axis before they contact the wheels, which is undesirable. In a nominal configuration, the maximum value of β is given as

$$\beta_{\max} = \tan^{-1}\left(\frac{0.5L_{\text{split}}}{\sqrt{r_{\text{wheel}}^2 - L_{\text{offset}}^2}}\right) \tag{6}$$

3.2 Design Optimization. A full factorial design optimization was performed using the objectives discussed in Sec. 2 (system kinematic isotropy, the ability of an ASOC module to maintain ground contact, and the maximum traversable obstacle height), and constraints outlined in Sec. 3.1 (workspace limitations, module interference, and maximum suspension travel). The optimization parameters are the number of ASOC modules, L_{split}, L_{offset}, r_{wheel}, and w_{wheel}. Objective function J is expressed as a sum of the normalized mobility parameters

$$J = \frac{K}{K^*} + \frac{\beta_{\max}}{\beta_{\max}^*} + \frac{h}{h^*} + \frac{d_{\max}}{d_{\max}^*} \tag{7}$$

where K is the kinematic isotropy, $\beta_{\max}$ is the maximum β axis pivot angle, h is the maximum traversable obstacle height, and $d_{\max}$ is the maximum traversable distance. The star superscript refers to the maximum value of each parameter in the design space. The optimization consisted of a full factorial analysis over the design space to maximize the value of J.

In this analysis, kinematic isotropy and the maximum pivot angle are calculated, as described in Secs. 2.2 and 3.1.2, respectively. The maximum traversable obstacle height is assumed to be a linear function of the wheel radius.

The optimization algorithm estimates maximum traversable dis-

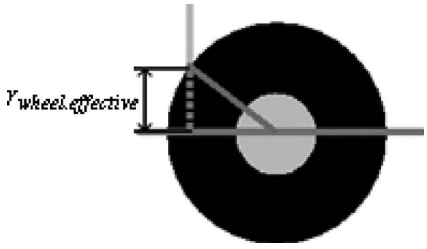

Fig. 16 Depiction of $r_{\text{wheeleffective}}$

tance by first determining the maximum available onboard energy. For the purposes of this study, it is assumed that the vehicle is powered by batteries with an energy density ρ_{energy} of 576 kJ/kg (similar to that of lithium-ion batteries) [23]. The maximum allowable onboard battery mass M_{battery} is the difference between the nonbattery mass (i.e., wheels, structural components, electronics, etc.) and the predetermined total allowable mass. The total allowable mass was chosen as 65 kg. Wheel and ASOC masses are computed as a function of their sizes.

The energy consumed during forward travel is then estimated using an expansion of a semiempirical formulation for compaction resistance on deformable terrain [24]. This expanded equation is valid for a greater range of sinkages than the more commonly used classical form upon which it is based

$$\text{CR} = \frac{n_{\text{wheels}}}{\left(1 - \frac{n}{3} + \frac{n}{10}(n-1) - \frac{n}{42}(n-1)(n-2) + \frac{n}{216}(n-1)(n-2)(n-3)\right)^{(2n+2/2n+1)} (n+1) w_{\text{wheel}}^{(1/2n+1)} \left(\frac{k_c}{w_{\text{wheel}}} + k_\phi\right)^{(1/2n+1)}} \left[\frac{3\frac{Mg}{n_{\text{wheels}}}}{\sqrt{r_{\text{wheel}}}}\right]^{(2n+2/2n+1)} \tag{8}$$

In Eq. (8), CR is the compaction resistance (N), M is the total vehicle mass (kg), n_{wheels} is the number of wheels (i.e., twice the number of ASOC modules), and n, k_c, and k_ϕ are the terrain physical constants (shown in Table 3 [25,26]). Note that this estimate holds for straight-line driving, and does not consider other resistive forces (such as bulldozing forces) or energy used by other onboard devices.

The maximum traversable distance is approximated as

$$d_{\max} = \frac{M_{\text{battery}} \rho_{\text{energy}}}{\text{CR}} \tag{9}$$

Since the optimization compares similar systems, motor and drivetrain efficiencies are assumed identical for all candidate designs, and therefore, are not considered in the calculations.

3.3 Design Optimization Results. Table 4 compares the values of the optimized mobility parameters of robots with three, four, and five ASOC modules. The robots were optimized for travel over sandy loam. Results are presented relative to the robot with three ASOC modules.

A robot with four ASOC modules has similar values of kinematic isotropy (K), maximum β axis pivot angle ($\beta_{\max}$), and maximum traversable obstacle height (h) as a three ASOC robot, however, adding the fourth module decreases available battery mass, and therefore decreases maximum traversable distance ($d_{\max}$). A fifth ASOC module requires smaller wheels, resulting in lower maximum traversable obstacle height, but higher maximum β axis pivot angle.

Table 5 shows the values of the optimized geometric parameters for a three ASOC robot. Optimized values were calculated for each of the four terrain types shown in Table 3, assuming travel through randomized rough terrain with an angle range of 0–30 deg. Table 6 shows the change in mobility parameter values for optimized designs compared with a baseline design with parameters determined by engineering judgment ($L_{\text{offset}}=0.15$ m, $L_{\text{split}}=0.20$ m, $r_{\text{wheel}}=0.15$ m, $w_{\text{wheel}}=0.03$ m). The baseline design is included for illustrative purposes to show that the design is amenable to optimization.

In all cases, the optimized offset lengths were slightly smaller than the wheel radii, which yielded large allowable β tilt angles. The L_{split} to L_{offset} ratios were all near 2.27:1, thus maximizing isotropy for the given terrain roughness range.

As presented, the optimized parameter values for the relatively deformable terrains (i.e., dry sand and snow) resulted in wheels with narrower widths, compared with those optimized for relatively rigid terrains (i.e., sandy loam and clayey soil). The thinner widths lead to decreased wheel weight. One could also minimize ground pressure by choosing a wider wheel with smaller radius,

Table 3 Terrain parameters

Terrain type	n	k_c (kPa/m^{n-1})	k_ϕ (kPa/m^n)
Dry sand	1.1	0.9	1523.4
Sandy loam	0.7	5.3	1515.0
Clayey soil	0.5	13.2	692.2
Snow	1.6	4.4	196.7

Table 4 Effect of number of ASOCs on mobility parameters

No. of ASOCs	K (%)	$\beta_{\max}$ (%)	h (%)	$d_{\max}$ (%)
3	0	0	0	0
4	0	0	0	−41.4
5	−2.2	16.2	−60.9	−52.9

Table 5 Geometric parameters from optimization

Terrain type	L_{offset} (m)	L_{split} (m)	r_{wheel} (m)	w_{wheel} (m)
Dry sand	0.144	0.325	0.148	0.090
Sandy loam	0.144	0.325	0.148	0.112
Clayey soil	0.134	0.306	0.139	0.133
Snow	0.144	0.325	0.148	0.054

Table 6 Mobility parameter increases from optimization

Terrain type	K (%)	$\beta_{\max}$ (%)	H (%)	$d_{\max}$ (%)
Dry sand	13.2	85.2	−1.4	18.1
Sandy loam	13.2	85.2	−1.4	29.5
Clayey soil	12.8	82.8	−7.4	31.9
Snow	13.2	85.2	−1.4	3.3

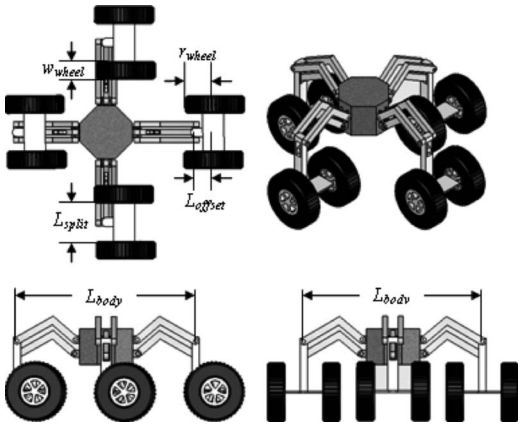

Fig. 17 A four view drawing of a point vehicle design

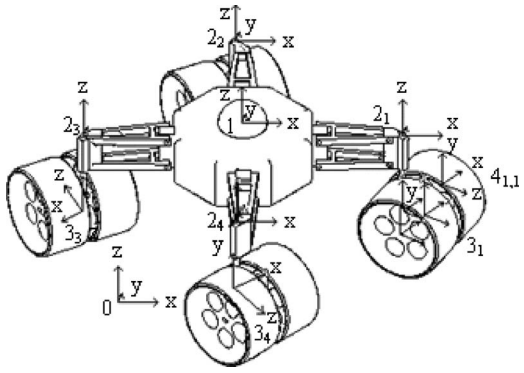

Fig. 18 Coordinate frame assignments for an ASOC-driven omnidirectional mobile robot. Some wheel and axle frames are hidden for clarity.

but for a given depth of sinkage, a tall, narrow wheel has significantly less compaction resistance than a short, wide one. For the relatively rigid terrains, a wider wheel was preferred as it allowed a greater onboard battery mass, thus increasing maximum traversable distance.

3.4 Point Vehicle Design. This section presents a point robot design with four ASOC modules (Fig. 17). This robot utilizes a four bar linkage suspension that achieves a maximum travel of 0.33 m. The wheels have a 0.163 m radius, the largest allowed, given a body length (L_{body}) of 1 m and the workspace constraints outlined in Sec. 3.1.1. A maximum pivot angle of 30 deg and high isotropy is achieved with an L_{split} of 0.21 m and an L_{offset} of 0.10 m (see Secs. 3.1.2 and 2.5) yielding $L_{\text{split}}/L_{\text{offset}}=2.1$.

4 Kinematic Analysis and Control

Section 3 presented the analysis of an ASOC-driven omnidirectional mobile robot for operation in rough terrain. During operation, control systems must coordinate ASOC motion while adapting to terrain unevenness. This section presents a kinematic controller that allows omnidirectional mobility in rough terrain.

4.1 Kinematic Analysis. Coordinate frames for an ASOC-driven omnidirectional mobile robot were defined using Denavit–Hartenberg (DH) notations shown in Table 7. Coordinate frame assignments are shown in Fig. 18.

In the notation above, d_i is the distance between frame i and frame $i+1$ along the z_{i+1} axis, ζ_i is the angle between x_i and x_{i+1} about the z_{i+1} axis, a_i is the distance from z_i to z_{i+1} along the x_{i+1} axis, ξ_i is the twist angle between z_i and z_{i+1} about the x_{i+1} axis, n is the ASOC number, m is the wheel number, r is the body radius, and h is the vertical distance from the ASOC base to the vehicle body.

Here, a three-dimensional model is considered. A body-fixed frame ("1") is allowed 6DOF with respect to an inertial frame ("0"). The interface of each ASOC module link and the robot body/suspension frame ("2_n," where n refers to the ASOC number, and N is the total number of ASOCs) is defined on the body at a distance r from the center of the body. A frame ("3_n") at the bottom of each ASOC module link is at a distance h below the previous frame, and can rotate about axis α. The next frame ("4_n") is defined on the axle at the midpoint between the wheels, and can rotate about β. For convenience, a frame is also defined at the center of each wheel ("$5_{n,m}$," where n refers to the ASOC number, and m refers to the wheel number). These redundant frames are fixed with respect to the axle frame. There is no specified wheel-ground contact frame, as each wheel may have no contact or several moving contact points.

Table 7 Joint representation in DH notation

Joint No.	d_i	ζ_i	a_i	ξ_i
1_n	0	$2\pi(n-1)/N$	r	0
2_n	h	$-(\alpha+\pi/2)$	0	$\pi/2$
3_n	L_{offset}	$-\beta$	0	0
$4_{n,m}$	0	0	$(-1)^m L_{\text{split}}/2$	0

Coordinate transformation matrices are defined as follows:

$$T_1^{2_n}=\begin{bmatrix}\cos(2\pi(n-1)/N) & -\sin(2\pi(n-1)/N) & 0 & r\\ \sin(2\pi(n-1)/N) & \cos(2\pi(n-1)/N) & 0 & 0\\ 0 & 0 & 1 & 0\\ 0 & 0 & 0 & 1\end{bmatrix} \tag{10}$$

$$T_{2_n}^{3_n}=\begin{bmatrix}\cos(-(\alpha_n+\pi/2)) & 0 & \sin(-(\alpha_n+\pi/2)) & 0\\ \sin(-(\alpha_n+\pi/2)) & 0 & -\cos(-(\alpha_n+\pi/2)) & 0\\ 0 & 1 & 0 & h\\ 0 & 0 & 0 & 1\end{bmatrix} \tag{11}$$

$$T_{3_n}^{4_n}=\begin{bmatrix}\cos(-\beta_n) & -\sin(-\beta_n) & 0 & 0\\ \sin(-\beta_n) & \cos(-\beta_n) & 0 & 0\\ 0 & 0 & 1 & L_{\text{offset}}\\ 0 & 0 & 0 & 1\end{bmatrix} \tag{12}$$

$$T_{4_n}^{5_{n,m}}=\begin{bmatrix}1 & 0 & 0 & (-1)^m\dfrac{L_{\text{split}}}{2}\\ 0 & 1 & 0 & 0\\ 0 & 0 & 1 & 0\\ 0 & 0 & 0 & 1\end{bmatrix} \tag{13}$$

where T_p^q is the matrix transforming motion from frame p into frame q. Thus, the transformation from the body center frame to the wheel n,m frame is

$$T_1^{5_{n,m}}=T_1^{2_n}T_{2_n}^{3_n}T_{3_n}^{4_n}T_{4_n}^{5_{n,m}} \tag{14}$$

Using these relations, the wheel velocities required to generate a desired body center velocity can be determined.

4.2 Kinematic Control. A simple kinematic control scheme was developed based on the preceding kinematic analysis. Given a desired body translational and rotational velocity defined in an inertial frame, the velocity for each ASOC wheel can be determined despite the effects of terrain unevenness.

First, the velocity of the link between the ASOC module and robot body is computed by

$$\dot{\mathbf{x}}_{\text{link}} = \dot{\mathbf{x}}_{\text{body}} + \dot{\boldsymbol{\varphi}} r \begin{bmatrix} \cos(\varsigma_i) \\ \sin(\varsigma_i) \end{bmatrix} \tag{15}$$

where $\dot{\mathbf{x}}_{\text{link}}$ and $\dot{\mathbf{x}}_{\text{body}}$ are the planar velocity vectors of the link and body, respectively, $\dot{\boldsymbol{\varphi}}$ is the yaw rate of the body, and r and ζ_i locate the link i in the body frame. Note that this control method aligns the thrust vectors of each ASOC with the direction of travel, minimizing internal forces. The wheel velocities that yield the desired ASOC link velocity are found as [19]

$$\dot{\mathbf{x}}_{\text{link}} = \begin{bmatrix} \frac{1}{2}\cos(\alpha_n) - \frac{L_{\text{offset}}}{L_{\text{split}}}\sin(\alpha_n) & \frac{1}{2}\cos(\alpha_n) + \frac{L_{\text{offset}}}{L_{\text{split}}}\sin(\alpha_n) \\ \frac{1}{2}\sin(\alpha_n) + \frac{L_{\text{offset}}}{L_{\text{split}}}\cos(\alpha_n) & \frac{1}{2}\sin(\alpha_n) - \frac{L_{\text{offset}}}{L_{\text{split}}}\cos(\alpha_n) \end{bmatrix} \times \begin{bmatrix} V_{n,1} \\ V_{n,2} \end{bmatrix} \tag{16}$$

and hence

$$\begin{bmatrix} V_{n,1} \\ V_{n,2} \end{bmatrix} = \begin{bmatrix} \frac{1}{2}\cos(\alpha_n) - \frac{L_{\text{offset}}}{L_{\text{split}}}\sin(\alpha_n) & \frac{1}{2}\cos(\alpha_n) + \frac{L_{\text{offset}}}{L_{\text{split}}}\sin(\alpha_n) \\ \frac{1}{2}\sin(\alpha_n) + \frac{L_{\text{offset}}}{L_{\text{split}}}\cos(\alpha_n) & \frac{1}{2}\sin(\alpha_n) - \frac{L_{\text{offset}}}{L_{\text{split}}}\cos(\alpha_n) \end{bmatrix}^{-1} \times \dot{\mathbf{x}}_{\text{link}} \tag{17}$$

where $V_{n,m}$ is the forward linear velocity of wheel n,m in the wheel frame ("$5_{n,m}$"), and is computed as $V_{n,m}=R\omega_{n,m}$, where R is the wheel radius, and $\omega_{n,m}$ is the wheel angular speed. Angular velocity is controllable via simple PD or other schemes.

Terrain roughness causes ASOC modules to tilt (i.e., rotate about β). Wheel velocities then possess nonzero components in the body's z dimension. The effects of module tilt can be compensated in the controller via computation of an effective L_{split} (see Fig. 11). The wheel velocity component in the body's x-y plane appears on the left side of Eq. (18). Inclusion of the effects of out of plane wheel velocity components in Eq. (17) yields

$$\begin{bmatrix} V_{n,1}\cos\gamma_{n,1} \\ V_{n,2}\cos\gamma_{n,2} \end{bmatrix} = \begin{bmatrix} \frac{\cos(\alpha_i)}{2} - \frac{L_{\text{offset}}}{L_{\text{split}}\cos(\beta_i)}\sin(\alpha_i) & \frac{\cos(\alpha_i)}{2} + \frac{L_{\text{offset}}}{L_{\text{split}}\cos(\beta_i)}\sin(\alpha_i) \\ \frac{\sin(\alpha_i)}{2} + \frac{L_{\text{offset}}}{L_{\text{split}}\cos(\beta_i)}\cos(\alpha_i) & \frac{\sin(\alpha_i)}{2} - \frac{L_{\text{offset}}}{L_{\text{split}}\cos(\beta_i)}\cos(\alpha_i) \end{bmatrix}^{-1} \dot{\mathbf{x}}_{\text{link}} \tag{18}$$

where $\gamma_{n,m}$ is the angle between the velocity vector of wheel n,m and the x-y plane in the body-fixed frame (see Fig. 19).

Figure 20 shows a block diagram of a scheme for rough terrain omnidirectional mobile robot control. The input is a desired velocity profile defined in the inertial frame. It is assumed that the robot's full state can be estimated. The desired velocity profile is converted to a desired velocity in the body-fixed frame based on the robot's current position and orientation. ASOC module link velocities are then computed via Eq. (15). Desired wheel velocities can then be calculated using Eq. (18), here, assuming knowledge or estimates of wheel-terrain contact angles. Wheel-terrain contact angles can be estimated via axle-mounted force sensors (to measure wheel-terrain interaction normal force direction) or via kinematic estimators [26]. PD controllers command each wheel to track the desired wheel velocities. Actual velocities can be determined via odometry; however, more sophisticated methods (such as visual odometry) are required to estimate wheel slip [27].

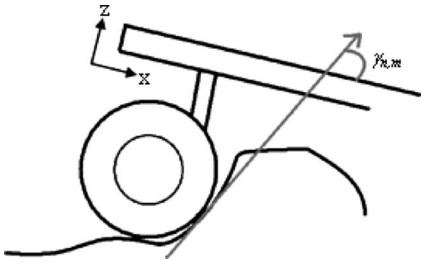

Fig. 19 Wheel-terrain contact angle $\gamma_{n,m}$. The gray vector is parallel to the velocity of the wheel.

4.3 Simulation Results. A dynamic model of an ASOC-driven mobile robot was developed to study the performance of the control method described above. The kinematic controller was implemented to allow the robot to track a desired velocity profile over rough terrain. Independent PD control loops allowed each wheel to track its desired velocity.

The robot parameters for the simulation were as follows: body length=1 m, total mass=65 kg, wheel radius=0.10 m, L_{split} =0.20 m, and L_{offset}=0.10 m. The control gains for each wheel were K_p=7.3 and K_d=0.02. Wheel-terrain interaction forces were determined via a simple coulomb friction model with μ=0.6. Terrain elevation was modeled as a triangularized mesh with elevation points possessing a standard deviation of σ. In initial simulations, it was assumed that the robot possessed perfect knowledge of wheel-terrain contact angles. Wheel-terrain contact locations were determined by making a thin wheel approximation and finding the intersection points between the wheel and the local triangular mesh patches.

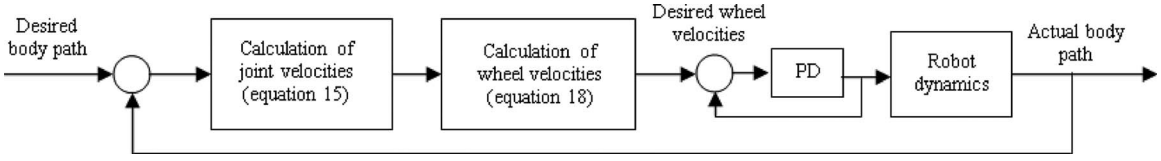

Fig. 20 Control scheme of an omnidirectional mobile robot

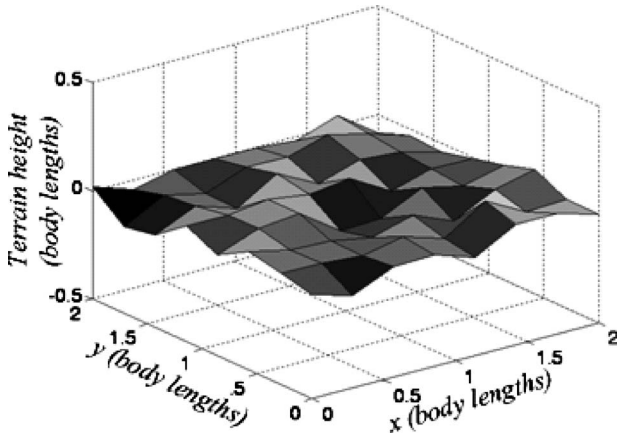

Fig. 21 Example of terrain used in simulation, with σ=4.5

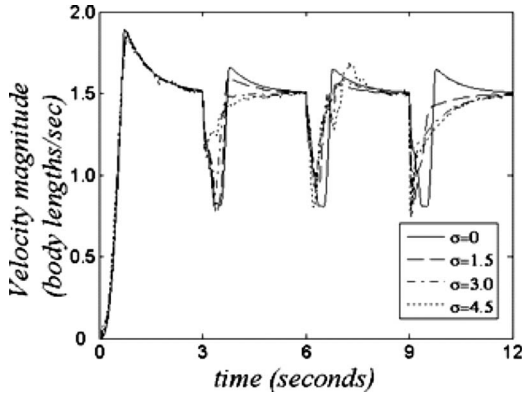

Fig. 23 Velocity magnitude during path tracking

To study the omnidirectional capability of the robot, a desired 4.5 m square path was commanded at a constant speed of 1.5 m/s. This corresponds to 1.5 body lengths/s.

In the following simulations, as shown in Fig. 21 σ was chosen as 0 cm, 1.5 cm, 3.0 cm, and 4.5 cm, yielding maximum terrain inclination angles of approximately 0 deg, 20 deg, 35 deg, and 45 deg, respectively.

In Fig. 22, it can be seen that the robot was able to track the desired path with good fidelity, even in very rough terrain. In these simulations, the controller had error and noise-free, continuous absolute position data. Table 8 presents the RMS error for this trial for each terrain roughness.

Although an omnidirectional robot can kinematically perform zero radius turns at any velocity, dynamic effects may reduce path tracking capability at higher velocities. Figure 23 shows that the vehicle is able to maintain a high velocity magnitude when the body was changing direction. During these simulations, the velocity never dropped below 48% of the nominal commanded velocity.

Further simulations were conducted to study the effects of utilizing wheel-terrain contact angle knowledge in the controller, and knowledge of robot absolute position. Simulations were run with and without absolute position updates at 0.5 Hz, and with and without knowledge of wheel-terrain contact angle. Simple dead reckoning was used to estimate vehicle position in simulations without absolute position knowledge, and to interpolate between updates in simulations with absolute position knowledge. Path tracking results are shown in Fig. 24. Numerical results are shown in Table 9.

Note that the path tracking error in simulations with absolute position information is bounded, while the tracking error in simulations without absolute position data is not. When absolute position information is not available, a 75.3% reduction in path tracking error is seen when the vehicle controller uses wheel-terrain contact angle information. This is useful for the many situations where position information from GPS, for example, may be unavailable. Even with absolute position updates, path tracking error is reduced by 60.7% when the controller wheel-terrain contact angle information.

5 Conclusions

In this paper, the design and control of an omnidirectional mobile robot driven by active split offset casters for use in rough terrain has been studied. An isotropy analysis was conducted to

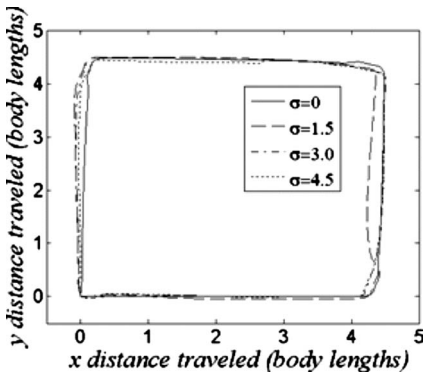

Fig. 22 Top view of robot path tracking a square on rough terrain

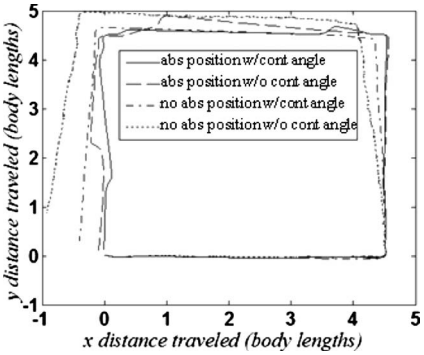

Fig. 24 Top view of the body trace during square tracking on rough terrain for varying levels of controller knowledge

Table 8 RMS path tracking error for several terrain heights

σ	RMS error (% body)
0.0	8.67
1.5	8.89
3.0	10.48
4.5	11.59

Table 9 RMS path tracking error for varying controller knowledge

Controller knowledge	RMS error (% body)
Absolute position with contact angle	6.96
Absolute position without contact angle	17.71
No absolute position with contact angle	21.28
No absolute position without contact angle	86.31

determine the optimal geometry and layout of the ASOC modules. This analysis indicates that equally spaced modules with $L_{split}/L_{offset}=2.0$ yield a robot with equal mobility capability in all directions on flat terrain. On rough terrain, a larger ratio is desired, and robot isotropy degrades slightly. It also shows that isotropy is independent of wheel radius, which increases the scalability of the design.

Numerous design considerations for omnidirectional mobile robots were presented. An optimization algorithm was implemented to derive values for ASOC module and wheel geometries. For illustration, a man-portable robot was designed, but the geometric constraints and the optimization algorithm are scalable and can be applied to robots of any size. It was shown that the designs suggested by the optimization have improved performance when compared with a nonoptimized design. Through deliberate ASOC geometric parameter selection, it was possible to increase estimated traverse distance and mobility versus a baseline design.

A kinematic controller was developed, and its performance was studied on both flat and rough terrain. The effects of wheel-terrain contact angle information and absolute position knowledge on performance were studied. Simulation results showed that an omnidirectional mobile robot is able to track a square trajectory with good performance, despite local terrain inclinations angles near 45 deg. It was also shown that substantial path tracking improvements were possible if wheel-terrain contact angle information was used in the controller.

References

[1] Fish, S., 2004, "UGV's in Future Combat Systems," *Proceedings of the SPIE–The International Society for Optical Engineering, Unmanned Ground Vehicle Technology VI*, Vol. 5422, pp. 288–291.

[2] Blitch, J., 1996, "Artificial Intelligence Technologies for Robot Assisted Urban Search and Rescue," Expert Systems with Applications, **11**(2), pp. 109–124.

[3] Erickson, J., 2006, "Living the Dream: An Overview of the Mars Exploration Project," IEEE Trans. Rob. Autom., **13**(2), pp. 12–18.

[4] Cheng, J., Gao, L., and Wang, H., 2006, "Steering Analysis of Tracked Vehicles Based on Skid Condition," Chin. J. Mech. Eng., **42**, pp. 192–195.

[5] Ishigami, G., Miwa, A., and Yoshida, K., 2005 "Steering Trajectory Analysis of Planetary Exploration Rovers Based on All-Wheel Dynamics Model," *Proceedings of the Eighth International Symposium on Artificial Intelligence, Robotics and Automation in Space*, pp. 121–128.

[6] Iagnemma, K., and Dubowsky, S., 2004, "Mobile Robots in Rough Terrain: Estimation, Motion Planning, and Control With Application to Planetary Rovers," *Springer Tracts in Advanced Robotics (STAR) Series*, Springer, New York, Vol. 12.

[7] Fujisawa, S., Ohkubo, K., Yoshida, T., Satonaka, N., Shidama, Y., and Yamaura, H., 1997, "Improved Moving Properties of an Omnidirectional Vehicle Using Stepping Motor," *Proceedings of the 36th Conference on Decision and Control*, San Diego, pp. 3654–3657.

[8] Williams, R., Carter, B., Gallina, P., and Rosati, G., 2002, "Wheeled Omni-Directional Robot Dynamics Including Slip," *Proceedings of the 2002 ASME Design Engineering Technical Conferences*.

[9] Muir, P., and Neuman, C., 1987 "Kinematic Modeling for Feedback Control of an Omnidirectional Wheeled Mobile Robot," *Proceedings of the 1987 IEEE International Conference on Robotics and Automation.*

[10] Bradley, A., Miller, S., Creary, G., Miller, N., Begley, M., and Misch, N., 2005, "Mobius, An Omnidirectional Robot Utilizing Mecanum Wheels and Fuzzy Logic Control," *Proceedings of the 28th Annual AAS Rocky Mountain Guidance and Control Conference*, pp. 251–266.

[11] Ferriere, L., and Raucent, B., 1998, "ROLLMOBS, A New Universal Wheel Concept," *Proceedings of the 1998 IEEE International Conference on Robotics and Automation*, Leuven, pp. 1877–1882.

[12] West, A. M., and Asada, H., 1997, "Design of Ball Wheel Mechanisms for Omnidirectional Vehicles With Full Mobility and Invariant Kinematics," ASME J. Mech. Des., **199**(2), pp. 153–161.

[13] Alexander, J. C., and Maddocks, J. H., 1989, "On the Kinematics of Wheeled Mobile Robots," Int. J. Robot. Res., **8**(5), pp. 15–27.

[14] Low, K. H., and Leow, Y. P., 2005, "Kinematic Modeling, Mobility Analysis and Design of Wheeled Mobile Robots," Adv. Rob., **19**, pp. 73–99.

[15] Gracia, L., and Tornero, J., 2007, "A New Geometric Approach to Characterize the Singularity of Wheeled Mobile Robots," Robotica, **25**, pp. 627–638.

[16] Carlson, J., and Murphy, R., 2005, "How UGVs Physically Fail in the Field," IEEE Trans. Rob. Autom., **21**(3), pp. 423–437.

[17] Wood, C., Davidson, M., Rich, S., Keller, J., and Maxfield, R., 1999, "T2 Omni-Directional Vehicle Mechanical Design," *Proceedings of the SPIE Conference on Mobile Robots XIV*, Boston, pp. 69–76.

[18] Park, T., Lee, J., Yi, B., Kim, W., and You, B., Oh, S., 2002, "Optimal Design and Actuator Sizing of Redundantly Actuated Omni-Directional Mobile Robots," *Proceedings of the IEEE International Conference on Robotics and Automation*, pp. 732–737.

[19] Yu, H., Dubowsky, S., and Skwersky, A., 2000, "Omni-Directional Mobility Using Active Split Offset Castors," *Proceedings of the 26th Biennial Mechanisms and Robotics Conference of the 2000 ASME Design Engineering Technical Conferences*.

[20] Spenko, M., Yu, H., and Dubowsky, S., 2002, "Analysis and Design of an Omnidirectional Platform for Operation on Non-Ideal Floors," *Proceedings of the 2002 IEEE International Conference on Robotics and Automation*, Washington, DC.

[21] Saha, K., Ángeles, J., and Darcovich, J., 1995, "The Design of Kinematically Isotropic Rolling Robots With Omnidirectional Wheels," Mech. Mach. Theory, **30**(8), pp. 1127–1137.

[22] Gracia, L., and Tornero, J., 2008, "Kinematic Models and Isotropy Analysis of Wheeled Mobile Robots," Robotica, **26**, pp. 587–599.

[23] Minami, T., Tatsumisago, M., and Wakihara, M., 2004, *Solid State Ionics for Batteries*, Springer-Verlag, Berlin.

[24] Bekker, G., 1956, *Theory of Land Locomotion, the Mechanics of Vehicle Mobility*, University of Michigan Press, Ann Arbor, MI.

[25] Yong, R., Fattah, E., and Skiadas, N., 1984, *Vehicle Traction Mechanics*, Elsevier, Amsterdam.

[26] Wong, J., 1989, *Terramechanics and Offroad Vehicles*, Elsevier, Amsterdam.

[27] Cheng, Y., Maimone, M., and Matthies, L., 2006, "Visual Odometry on the Mars Exploration Rovers," IEEE Rob. Autom. Mag., **13**(2), pp. 54–62.